nature materials

ARTICLES

https://doi.org/10.1038/s41563-020-0800-y

Check for updates

Insight into the effects of confined hydrocarbon species on the lifetime of methanol conversion catalysts

I. Lezcano-Gonzalez[1,2]✉, E. Campbell[1,2], A. E. J. Hoffman[3], M. Bocus[3], I. V. Sazanovich[4], M. Towrie[4], M. Agote-Aran[1,2], E. K. Gibson[1,2,5], A. Greenaway[1,2], K. De Wispelaere[3], V. Van Speybroeck[3]✉ and A. M. Beale[1,2]✉

The methanol-to-hydrocarbons reaction refers collectively to a series of important industrial catalytic processes to produce either olefins or gasoline. Mechanistically, methanol conversion proceeds through a 'pool' of hydrocarbon species. For the methanol-to-olefins process, these species can be delineated broadly into 'desired' lighter olefins and 'undesired' heavier fractions that cause deactivation in a matter of hours. The crux in further catalyst optimization is the ability to follow the formation of carbonaceous species during operation. Here, we report the combined results of an operando Kerr-gated Raman spectroscopic study with state-of-the-art operando molecular simulations, which allowed us to follow the formation of hydrocarbon species at various stages of methanol conversion. Polyenes are identified as crucial intermediates towards formation of polycyclic aromatic hydrocarbons, with their fate determined largely by the zeolite topology. Notably, we provide the missing link between active and deactivating species, which allows us to propose potential design rules for future-generation catalysts.

Small olefins are highly important platform chemicals because they are 'building blocks' for the global polymer and plastic market and lead to a propylene market that is worth US$90 billion a year (see www.transparencymarketresearch.com/ethylene-and-propylene.html). Steam cracking of light hydrocarbons or naphtha typically produces ethylene, whereas fluid catalytic cracking of naphtha produces propylene. Alternative, sustainable routes to olefin production are necessary to omit crude oil as a source, and require new process technologies and catalytic materials. Alternative sources for olefin production include coal, natural gas and sustainable materials (for example, second-generation biomass); such production can be realized at a large scale through a multistep process that involves methanol synthesis from syngas followed by a methanol-to-hydrocarbons (MTH) process using zeolites[1–3]. Many variants of the MTH process have been commercialized and it remains a vital technology for the production of chemicals and fuels, especially in a variable window of operation in terms of feed or product distribution. The scope to influence MTH products by altering parameters such as reaction conditions (temperature and flow) and zeolite properties (topology and acidity) is particularly attractive. These variables sway product selectivity between the extremes of gasoline (methanol-to-gasoline, or MTG) and light olefins (methanol-to-olefins, or MTO)[1,2]. Catalyst stability is perhaps the main challenge for the widespread use of this technology, specifically the fast formation of carbon deposits during operation that severely compromises process efficacy[1,4–6]. For small-pore zeolites, deactivation occurs in a matter of hours. Despite intensive research efforts, a comprehensive molecular insight into deactivation phenomena remains absent, but such insight is necessary to improve process efficiency. The presence of many intermediate species and the need to track them under reaction conditions renders this work very challenging[1,2,4].

The MTH reaction has been shown to proceed through an indirect hydrocarbon pool mechanism in which organic molecules that are confined within zeolite micropores act as reaction centres to which methanol is added and olefins are split off through dealkylation and cracking steps (Fig. 1a)[1,7,8]. There is consensus that methylated benzenes and olefins are key hydrocarbon pool species in both CHA and MFI zeolite topologies, whereas polycyclic aromatic hydrocarbons (PAHs) are related to catalyst deactivation, blocking zeolite pores and forming carbon deposits[1,4,7–11]. Recent studies have shown that altering the catalyst structure and/or acidity, as well as co-feeding of H_2, can improve the lifetime[3,12,13], but how the plethora of adsorbed species affects this is unclear. Most mechanistic insight has been gleaned from NMR[14–17], Raman[18–20], infrared[9,21,22] and ultraviolet–visible spectroscopic studies[22–24], some of which were used under in situ or operando conditions, as well as from theoretical calculations[10,25]. Studies that can truly discriminate between essential species and deactivating species in the catalytic process are very limited[14,19,20,22–24,26], with time- and temperature-resolved studies most suited to unravelling this complexity. To progress further in controlling catalytic performance, a deep mechanistic understanding of the formation and evolution of the hydrocarbon pool species under operating conditions is needed.

Here, we combine operando Kerr-gated Raman spectroscopic studies with advanced simulation tools to follow the formation of carbonaceous species during methanol conversion. Raman spectroscopy is a powerful technique for characterizing carbon species under reaction conditions, but its application to zeolite catalysts is often hindered by inherent and incidental fluorescence from the sample[27]. To some extent, this can be circumvented with the use

[1]Chemistry Department, University College London, London, UK. [2]UK Catalysis Hub, Research Complex at Harwell, Didcot, UK. [3]Center for Molecular Modeling, Ghent University, Zwijnaarde, Belgium. [4]Central Laser Facility, STFC, Research Complex at Harwell, Didcot, UK. [5]School of Chemistry, University of Glasgow, Glasgow, UK. ✉e-mail: i.lezcano-gonzalez@ucl.ac.uk; veronique.vanspeybroeck@ugent.be; Andrew.beale@ucl.ac.uk

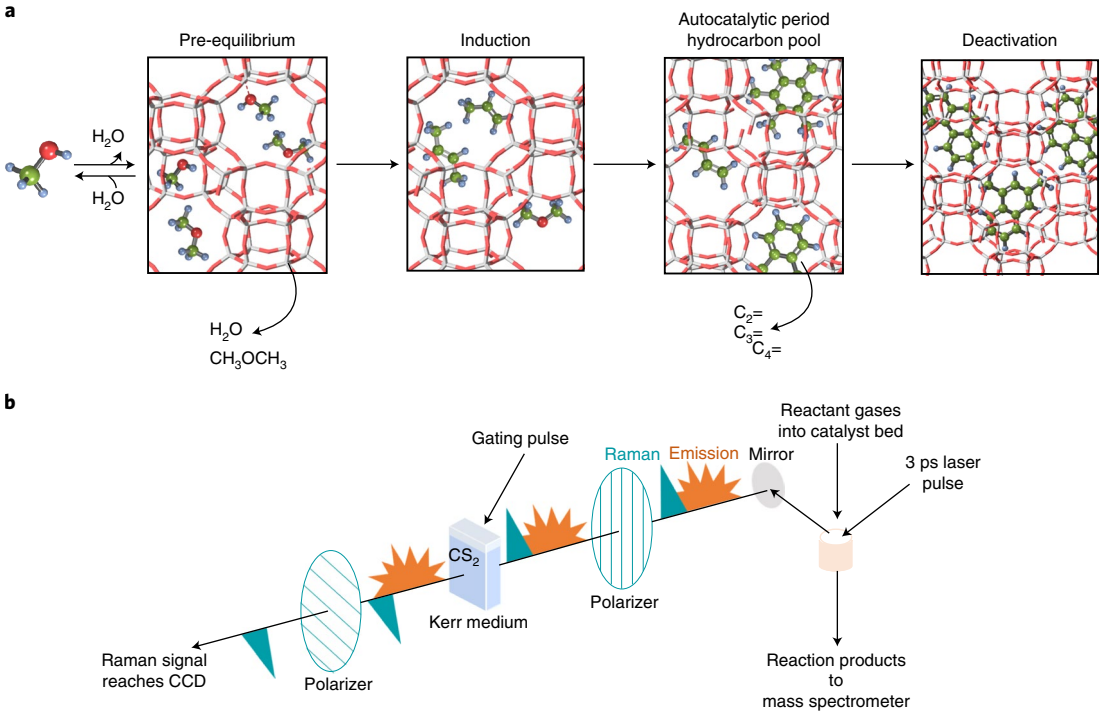

Fig. 1 | Different stages of the MTO reaction and the Kerr-gate Raman spectroscopy set-up. a, Illustration of different stages of the MTO reaction on CHA-type zeolite materials, with the corresponding adsorbed intermediates and outlet products. **b**, Representation of the Kerr gate that blocks fluorescence from the sample. This technique makes use of the difference between fluorescence and Raman temporal behaviour to temporally reject fluorescence; the Raman process is instantaneous and limited by the laser pulse, whereas fluorescence occurs on longer time scale of 10^{-6} s to 10^{-9} s (see Supplementary Information for details). CCD, charge coupled device.

of differing excitation wavelengths, although it is at the expense of either a weaker Raman signal (infrared source) or a higher energy load on the sample (ultraviolet source), which can cause photodegradation[27,28]. An interesting alternative is to use a visible excitation source combined with a Kerr-gated spectrometer, which discriminates between the Raman signal and fluorescence based on the temporal differences between the two processes (Fig. 1b and Supplementary Fig. 1)[29,30]. Furthermore, as many key molecular 'protagonists' in the reaction pathway are coloured[22,23], the phenomenon of resonance enhancement of the Raman signal (enhancement of up to 10^8) allows us to detect species that are normally not observable in this reaction[27,28]. The benefit of performing Kerr-gated Raman spectroscopy versus conventional Raman spectroscopy is demonstrably clear (Supplementary Fig. 2). Operando molecular simulations identified reaction intermediates and determined their mobility within the zeolite host. The combined experimental and theoretical approach allowed us to piece together the hydrocarbon evolution within two of the best-studied zeolite topologies: CHA and MFI. We identified, as a principal finding, the crucial role of polyenes and show that their fate is dependent on the zeolite topology. Within the CHA topology, polyenes are precursors for deactivating PAH species.

Early stages of the MTO reaction: pre-equilibrium stage and initiation of the induction period (100–260 °C)

The evolution of hydrocarbon species that are formed during the MTO reaction on SSZ-13 (a zeolite with CHA topology) was examined by operando Kerr-gated Raman spectroscopy combined with real-time product analysis by mass spectrometer (see Methods and Supplementary Table 1 for details). Data were recorded up to 450 °C (Figs. 2, 5 and Supplementary Figs. 3,4). Between 100 °C and 240 °C, a gradual decrease in the Raman bands of methanol (2,954 cm^{-1} and 2,855 cm^{-1} (C–H ν_{as} and ν_s), 1,455 cm^{-1} (CH_3 δ) and 1,006 cm^{-1} (C–O ν)) was observed (Supplementary Figs. 3,4), and dimethyl ether and water were detected by mass spectrometry in the reactor outlet stream (Supplementary Fig. 4). These products are characteristic of the pre-equilibrium stage of the reaction (Fig. 1)[31] in which methanol is dehydrated into a mixture of methanol, dimethyl ether and water. Note that methanol bands in the experimental spectra are in agreement with the simulations (Supplementary Figs. 5–8 and Supplementary Table 2). At 240–260 °C the bands of methanol were barely observed (Fig. 2a), and a new weak signal was detected at 1,600–1,625 cm^{-1} that, according to previous work[32,33] and our simulations (Fig. 3a and Supplementary Figs. 9–11), can be assigned to stretching modes of isolated C=C bonds, which indicates the onset of alkene formation and possibly small polyenes. These observations are consistent with the formation of the first hydrocarbons[15], which represents the beginning of the induction period and the build-up of hydrocarbon pool species within zeolite micropores (Fig. 1).

Identification of hydrocarbon pool intermediates (270–280 °C)

Further temperature increase led to a substantial increase in methanol conversion with a maximum at 283 °C, and to the formation of C_2–C_4 products (Fig. 2b), which is characteristic of the autocatalytic stage (Fig. 1). Accordingly, intense Raman bands were observed in the spectra at 270–280 °C that are attributable to various hydrocarbon pool species. Previous work in conjunction with our simulations (Fig. 3 and Supplementary Fig. 12)[18,32,33] identified bands at approximately 1,608 and 1,519 cm^{-1} (C=C ν_s and ν_{as}), 1,375 cm^{-1} (CH_3 δ), 1,265 cm^{-1} (C–H rock), 1,182 cm^{-1} (aromatic C–C ν modes) and 576 cm^{-1} (alkyl aromatic ring C–C δ). We attribute the origin of these bands to methylated benzenium ions that are now readily observable owing to resonance enhancement[16,23]. We note

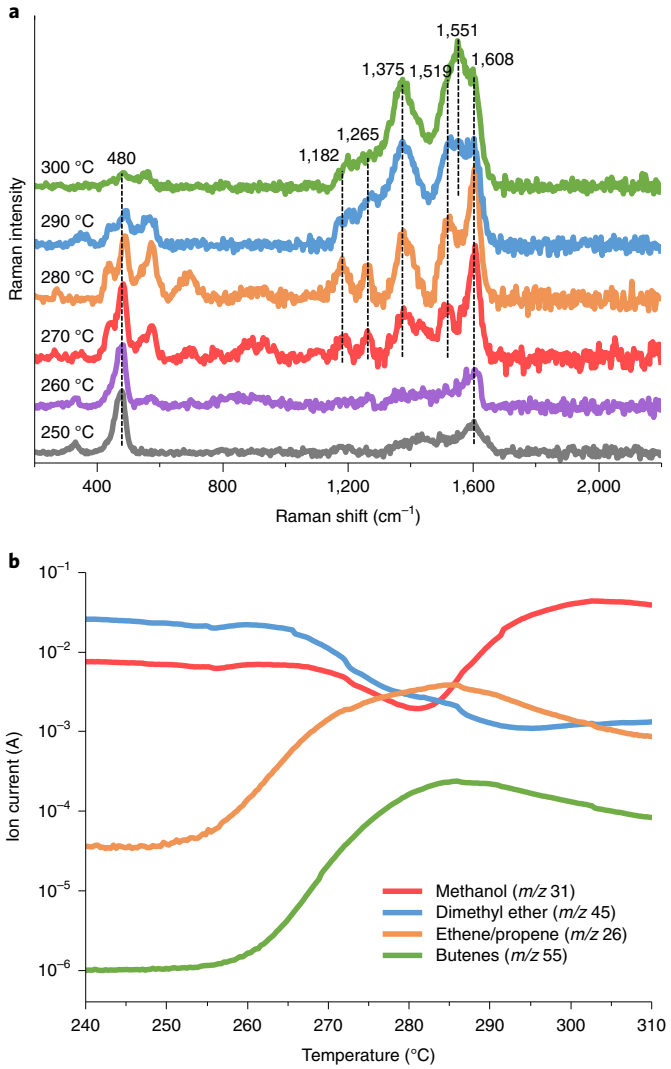

Fig. 2 | Operando Kerr-gated Raman spectroscopy of SSZ-13 zeolite during the MTO reaction; formation of hydrocarbon pool intermediates and onset of deactivation. a, Kerr-gated Raman spectra of SSZ-13 zeolite during the MTO reaction between 250 °C and 300 °C. Measurements were performed at increasing reaction temperatures. Raman bands are observed at 1,608 cm^{-1} (C=C ν_s), 1,551 cm^{-1} (conjugated π-system C=C ν), 1,519 cm^{-1} (C=C ν_{as}), 1,375 cm^{-1} (CH_2 or CH_3 δ, ring-breathing mode), 1,265 cm^{-1} (C–H rock), 1,182 cm^{-1} (C–C ν), 576 cm^{-1} (C–C δ) and 480 cm^{-1} (zeolite T–O bend vibration). Excitation wavelength, 400 nm; heating rate, 1 °C min^{-1}; weight of feed flowing per unit weight of the catalyst per hour, 1.6 $g_{methanol}\ g_{catalyst}^{-1}\ h^{-1}$. **b**, Mass traces of methanol and the reaction products. *M*/*z*, mass-to-charge ratio.

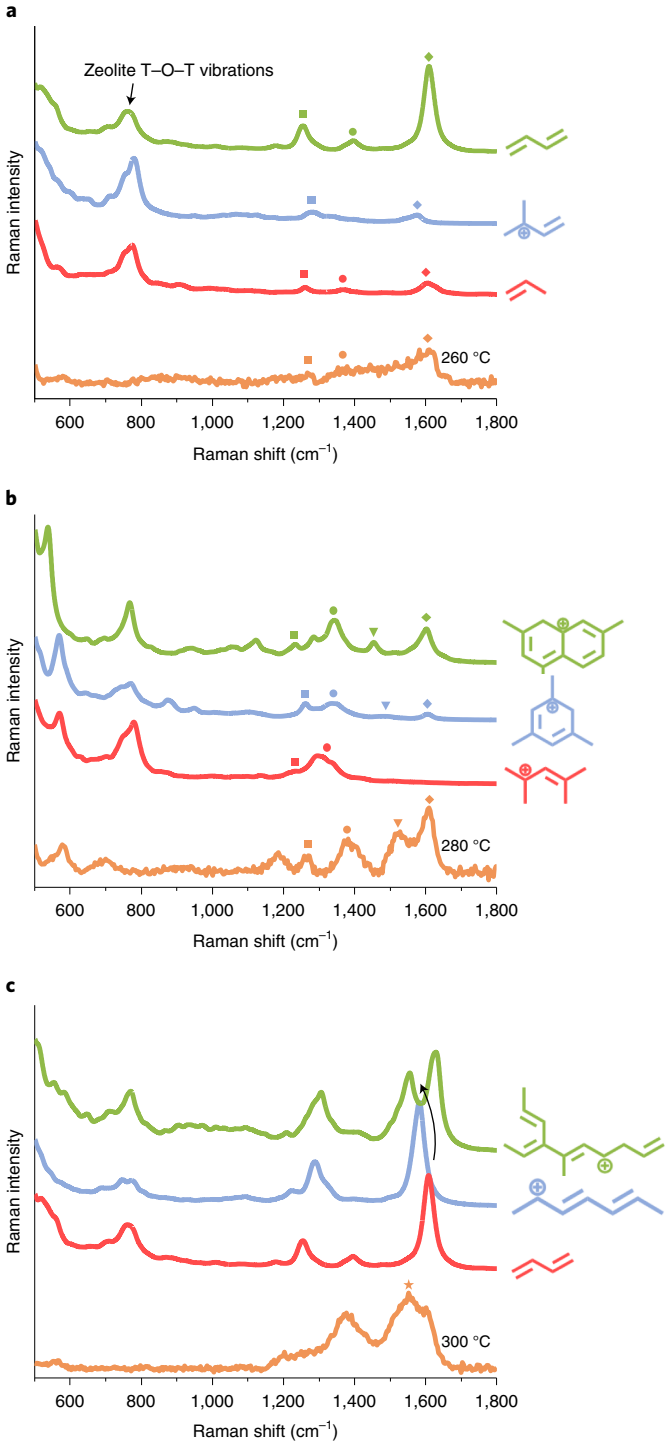

Fig. 3 | Comparison of experimental and simulated Raman spectra. **a**, Simulated Raman spectra of SSZ-13 zeolite that is loaded with model alkenes and small polyenes (red, blue and green) versus experimental Raman spectrum (orange) acquired during the MTO reaction at 260 °C. **b**, Simulated Raman spectra of SSZ-13 zeolite that is loaded with model dienyl, benzene and naphthalene species (red, blue and green) versus experimental Raman spectrum (orange) acquired during the MTO reaction at 280 °C. **c**, Simulated Raman spectra of SSZ-13 zeolite that is loaded with model polyenes (red, blue and green) versus experimental Raman spectrum (orange) acquired during the MTO reaction at 300 °C. Protonated structures are indicated with a + sign. Symbols (squares, circles, triangles and stars) highlight the main characteristic vibrations. (See Supplementary Information for the full assignments and the simulated spectra of additional model alkenes, polyenes and aromatic species.)

the excellent correspondence between our experiments and theoretical simulations (Fig. 3b and Supplementary Fig. 12).

Our simulations identified contributions from additional species besides alkenes, small polyenes and methylated benzenium ions. Specifically, Raman bands around 550 cm^{-1} (C–C δ) and in the 1,250–1,400 cm^{-1} range (C–H rock, CH_2 δ and CH_3 δ) are characteristic of dienylic cations (Fig. 3 and Supplementary Fig. 9) that can be formed either from dienes by protonation and subsequent hydride abstraction or by the reaction of monoenyl carbocations and olefins. The identification of (methylated) naphthalene(s) is more challenging. We note that the 1,375 cm^{-1} band is sufficiently broad and tall to contain multiple contributions including, as predicted by theory (Fig. 3 and Supplementary Fig. 12) and as identified in

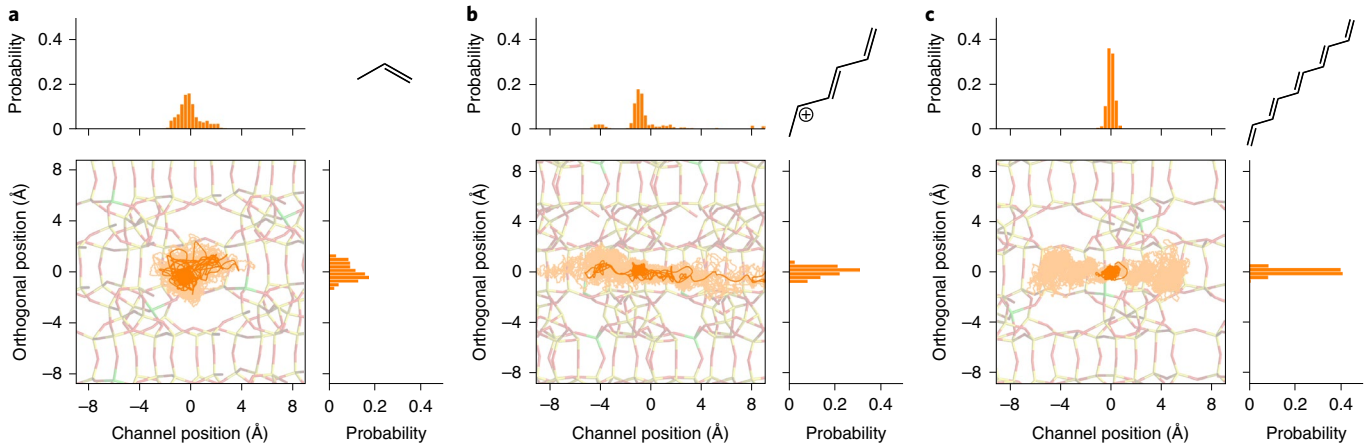

Fig. 4 | Mobility of polyene species that are formed at the onset of deactivation. a–c, Position of the COM of the intermediate (dark orange) and the positions of the carbon atoms (light orange) projected onto one of the 8-ring channels (horizontal axis) and a direction perpendicular to it (vertical axis), for propene (**a**), heptatriene (**b**) and decapentaene (**c**). The amount of time the COM resides at a certain position is illustrated by histogram plots. Protonated structures are indicated with a + sign.

previous work[32], a ring-breathing mode of naphthalenes along with CH_3 δ modes. From these observations, we conclude that methylated benzenium ions, along with alkenes, small polyenes, dienylic cations and possibly (methylated) naphthalene(s), are the hydrocarbon pool species that form on SSZ-13 during the induction period and are present in the autocatalytic stage of the reaction.

Confined hydrocarbon species at the onset of deactivation (290–300 °C)

Coincident with decreasing methanol conversion at 290 °C, a new intense band at 1,551 cm^{-1} emerged in the C=C stretch region of conjugated olefins (Fig. 2). Bands in this region were previously observed during conversion of methanol, dimethyl ether and light olefins, and were tentatively assigned to polyene-type species[18,21,32]. However, their high reactivity has prevented the study of zeolite-adsorbed polyenes and their unambiguous identification. To gain definitive insight into the species present, vibrational signatures of a number of polyene species were calculated (Fig. 3c and Supplementary Figs. 9–11,13–19). For linear polyenes with either straight or curled topologies, four characteristic vibrations were identified, including the stretching mode of the conjugated π-system (1,520–1,580 cm^{-1}), which red-shifted with increasing chain length. Branched polyenes showed an additional feature at 850–1,000 cm^{-1} owing to the out-of-plane wagging of C–H bonds. The absence of this mode in the experimental spectrum along with the stretching frequency of the conjugated π-system identify extended polyenes with no or small branches (Fig. 3c and Supplementary Figs. 9–11).

As the reaction progressed, a substantial growth of the 1,551 cm^{-1} band was observed at 300 °C. No additional features were detected in the 850–1,000 cm^{-1} region (Fig. 3). The intensification of the 1,551 cm^{-1} band accompanied an important decrease in methanol conversion (Fig. 2b) revealed a direct correlation between the formation of extended polyenes and the onset of catalyst deactivation, which is likely associated with confinement-induced effects on the mobility of these large molecules.

Mobility of hydrocarbon species formed during onset of activation and deactivation

So far, it remains unclear whether the detected carbonaceous species block the zeolite pore system or remain mobile. First-principle molecular dynamics simulations allowed us to examine the mobility of detected hydrocarbons within the zeolite pores (Supplementary Figs. 20–33). We followed the path of the centres of mass (COMs) of the carbon atoms during molecular dynamics runs of 40 ps at 350 °C, projecting the COMs onto the different channels as the reaction intermediates are expected to move along channels in the zeolite. The resulting mobilities and the projections of all carbon atom positions in the channel are visualized in two-dimensional plots (Fig. 4 and Supplementary Figs. 21,25,28,30 and 31). Marked differences in mobility for the various hydrocarbon pool species were observed. With small alkenes, simulations indicated no obvious impediments to their mobility, although a lack of preferred propagation direction reduced their probability of travelling through the pores by means of the 8-ring (Fig. 4a and Supplementary Fig. 25). It is well known that primary product diffusion through 8-rings is hindered[5,34]. By contrast, small, branched polyenes (for example, isoprene and vinylpentadiene) showed reduced mobility, particularly once they become branched (Supplementary Fig. 25). Interestingly, medium-length linear structures, such as heptatriene, exhibited the greatest mobility along the channels, which was characterized by the displacement of its COM by ~15 Å along the channel (Fig. 4b and Supplementary Fig. 22). The high mobility along a certain direction is the result of the linearity of the molecule. The length of heptatriene approaches the size of the cell, but the heptatriene still fits through the 8-rings. The molecule aligns itself with the channel (Supplementary Fig. 23) probably owing to the presence of Brønsted sites that facilitate its propagation along the channel. A COM displacement of ~5 Å for octatetraene suggested that this molecule is too long to travel through the pores, and decapentaene showed almost no mobility (Fig. 4c and Supplementary Fig. 24) as it curled around an 8-ring and became ensconced between two neighbouring cells, which inhibited further diffusion. Consistent with Kerr-gated Raman spectroscopy findings, the limited mobility that is observed for extended polyenes indicates their key role in catalyst deactivation.

Formation of polycyclic aromatic hydrocarbons (310–450 °C)

A further increase in temperature (Fig. 5a) led to the evolution of distinctive low-frequency bands (629–1,100 cm^{-1}) and more subtle changes in the intensities of bands between 1,250 cm^{-1} and 1,608 cm^{-1}. Based on our simulations, these features are consistent with the formation of PAHs (Fig. 5b and Supplementary Fig. 12). The decreased relative intensity of the 1,608 cm^{-1} (C=C ν_s) shoulder is probably owing to the consumption of small alkenes or polyenes and/or methylated benzenium ions. PAHs also present a band around this frequency (Fig. 5b), but these are less resonant than the

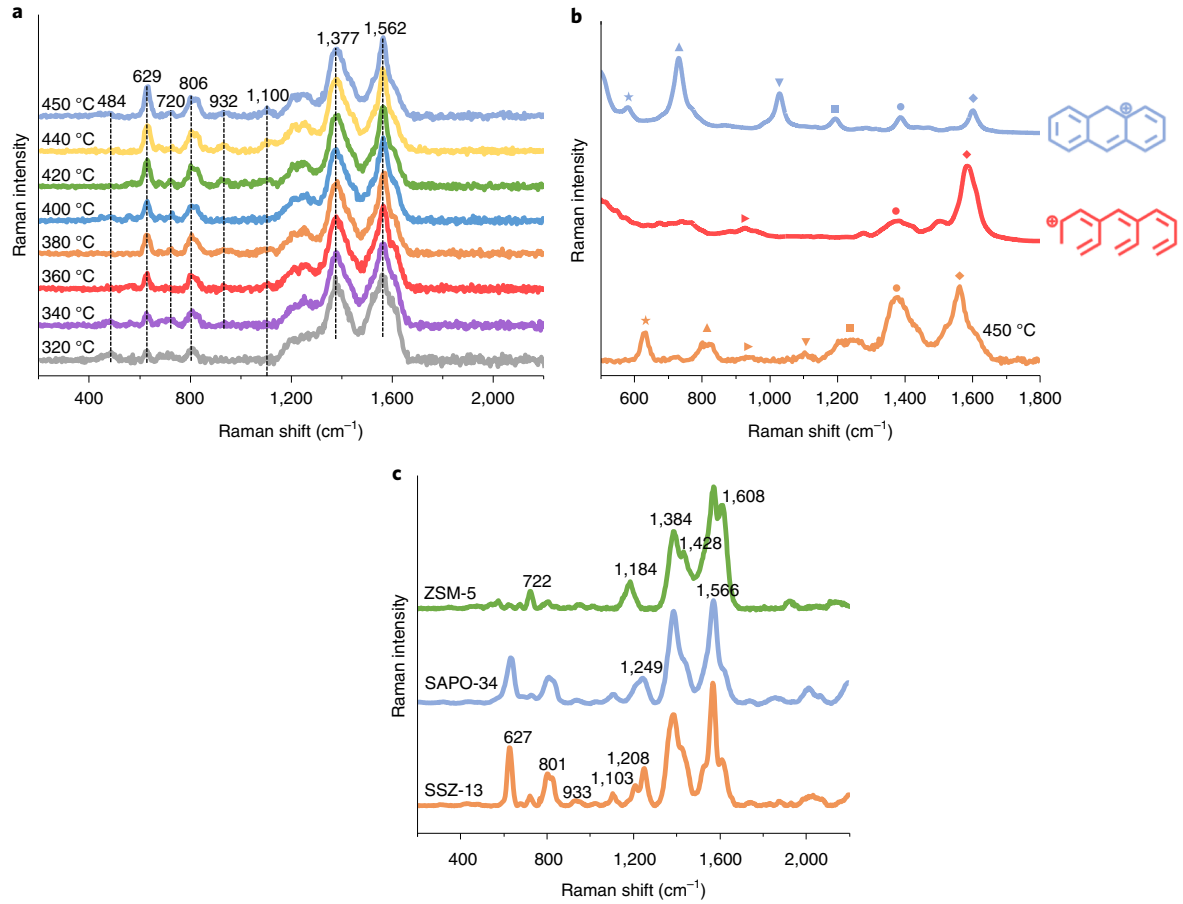

Fig. 5 | Operando Kerr-gated Raman spectroscopy of SSZ-13 zeolite during the MTO reaction; formation of PAHs and comparison with ZSM-5 and SAPO-34 archetypal MTH catalysts. a, Kerr-gated Raman spectra of SSZ-13 zeolite during the MTO reaction between 320 °C and 450 °C. Measurements performed at increasing reaction temperatures. Raman bands are observed at 1,608 cm^{-1} (C=C ν_s), 1,562 cm^{-1} (conjugated π-system C=C ν), 1,377 cm^{-1} (CH_2 or CH_3 δ, ring-breathing mode), 1,265 cm^{-1} (C–H rock), 629–1,100 cm^{-1} (ring-opening vibrations) and 480 cm^{-1} (zeolite T–O bend vibration). Excitation wavelength, 400 nm; heating rate, 1 °C min^{-1}; weight of feed flowing per unit weight of the catalyst per hour, 1.6 $g_{methanol}\, g_{catalyst}^{-1}\, h^{-1}$. **b**, Simulated Raman spectra of SSZ-13 zeolite loaded with a model polycyclic aromatic (anthracene, blue) and its precursor (red) versus experimental Raman spectrum acquired during the MTO reaction at 450 °C (orange). Protonated structures are indicated with a + sign. Symbols (stars, up-triangles, down-triangles, squares, circles, triangles, diamonds and side-triangles) highlight the main characteristic vibrations. (See Supplementary Information for the full assignments and the simulated spectra of additional model alkenes, polyenes and aromatic species.) **c**, Kerr-gated Raman spectra of SSZ-13, SAPO-34 and ZSM-5 catalysts recorded at room temperature (21 °C) after quenching the reaction at 450 °C.

species being consumed, which leads to a decrease in signal intensity. In addition, a decrease in the zeolite bands, which essentially vanish by 360 °C, indicates substantial hydrocarbon accumulation owing to increased absorption (gradual sample darkening) of the incident excitation beam[35].

Our mobility studies revealed that branched polyenes block the CHA pore system. During a regular molecular dynamics run at 350 °C of an exemplar branched polyene (3,4-divinylhexa-1,3,5-triene), we observed spontaneous intramolecular cyclization that formed a new ring-type species (in this case, 3,4-diethyl-2-methylcyclopentenium ion). This observation establishes a clear link between the presence of polyenes and the eventual formation of PAHs (Supplementary Fig. 13). To assess whether this propensity towards cyclization is intrinsic to all polyenes irrespective of their degree of branching, we performed additional molecular dynamics simulations on the non-branched, 6-protonated 1,3,5-heptatriene at 350 °C. When starting from a *cis* configuration for the C_1–C_2 and C_2–C_3 bonds, we observed spontaneous cyclization in all simulations (Supplementary Fig. 34a), which confirms that intramolecular cyclization from the *cis,cis* conformation is basically barrier-free. Steric hindrance between the C_1 and the C_5 hydrogens explains the high reactivity of the *cis,cis* conformation, prevents the π-system from being fully coplanar, and substantially reduces the delocalization of the positive charge (Supplementary Fig. 34b). However, linear, non-branched polyenes must overcome an energetic penalty to isomerize the C_1–C_2 and C_2–C_3 bonds from the stable *trans,trans* to the reactive *cis,cis* conformation. For non-branched polyenes, this barrier equals 55 kJ/mol, whereas highly branched polyenes have no energetic barrier to form the pre-reactive complex for intramolecular cyclization (Supplementary Figs. 35,36). We conclude that branched polyenes that are formed in the zeolite pores immediately cyclize, whereas linear polyenes survive longer owing to the energetic penalty to form the reactive *cis,cis* isomers.

Besides intramolecular cyclization, ring-forming routes from extended polyenes comprise electrophilic aromatic substitution of single-ring aromatics or the Diels–Alder reaction between polyenes and alkenes, both of which are followed by intramolecular rearrangement steps (Supplementary Fig. 37). In view of the concomitant consumption of small alkenes or polyenes and methylated benzenium ions in this temperature range (which is the cause of the decreased band intensity at 1,608 cm^{-1}), it is likely that these other processes also occur. Once extended PAHs form, they block the

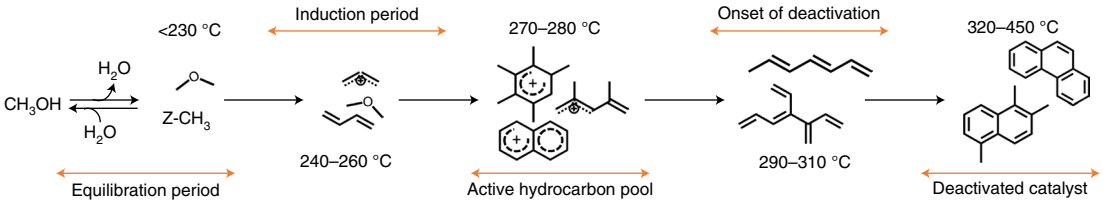

Fig. 6 | Hydrocarbon species evolution during the MTO reaction on small-pore catalyst materials. Different hydrocarbon pool species are formed during the induction period of the MTO reaction, including alkenes, small polyenes, dienylic cations, methylated benzenium ions and possibly (methylated) naphthalene(s), which are responsible for the formation of C_2–C_4 alkenes in the period of maximum methanol conversion. The formation of polyenes with no or small branches (for example, decapentaene), which show almost no mobility and curl around the 8-ring of the zeolite framework, leads to an important decrease in activity; this decrease is likely related to reduced diffusivity of both reactant and products. Subsequently, PAHs that are formed from polyenes (possibly) through intramolecular cyclization start to accumulate on the catalyst surface.

CHA cage, as demonstrated by a mobility analysis (Supplementary Figs. 28,29). Therefore, operando Kerr-gated Raman spectroscopy is able to identify initial polyene formation, and to track their consumption and consequent transformation into PAHs. This is observed under both variable-temperature (Fig. 2) and isothermal conditions (Supplementary Fig. 38). We propose, therefore, that deactivation of CHA materials occurs through cage blocking, first by extended polyenes and subsequently, as these polyenes react, by PAH species.

Effect of zeolite topology on intermediates formation

Similar results were obtained during the MTH process over ZSM-5 (a zeolite with MFI topology), although formation of hydrocarbon pool species occurred at higher temperatures (300 °C; Supplementary Fig. 39a). Above 300 °C, features at 1,605 cm^{-1}, 1,522 cm^{-1}, 1,383 cm^{-1}, 1,265 cm^{-1}, 1,179 cm^{-1} and 564 cm^{-1} were observed that were assigned to methylated benzenium ions, dienyl carbocations and possibly (methylated) naphthalene(s). Simultaneously, the mass spectrometry showed a gradual increase in the conversion of methanol and in the formation of olefins and aromatics (Supplementary Fig. 39b). At 330 °C, polyenes are formed (signal at 1,552 cm^{-1}) without any effect on activity. Also in contrast to SSZ-13, the lower relative intensity of this band at 1,605 cm^{-1} (C=C ν_s) suggests that among the species detected, methylated benzenium ions dominate. Importantly, further heating to 450 °C (Supplementary Fig. 39c) did not induce PAH formation, which is consistent with previous reports that PAHs do not build up substantially within ZSM-5 micropores at this stage[36], and no decrease in methanol conversion or product formation was observed by mass spectrometry. We propose that in the larger-channelled ZSM-5, linear polyenes diffuse relatively unimpeded and prevent catalyst deactivation through blocking. Considering the larger void volume of the chabazite cage compared with the ZSM-5 channel intersections[37], steric constraints may also play a role by inhibiting polyene cyclization on the MFI topology and preventing PAH formation. The zeolite band at 360 cm^{-1} also did not decrease, which indicates a diminished accumulation of hydrocarbons compared to SSZ-13. Note, however, that owing to the increased lifetime of this material[36], we cannot rule out that at longer reaction times, polyenes may contribute to deactivation.

Spent catalysts

At 450 °C, the reactions were quenched to record several scans at room temperature (21 °C) (Fig. 5c). Again, no clear features of PAHs were seen for ZSM-5, which supports the concept that, if present, only small amounts of PAHs are formed on this catalyst, probably on the external zeolite surface[38]; by contrast, SSZ-13 showed a number of intense low-frequency peaks that were attributable to PAHs. For comparison, data are also given for SAPO-34 (a silicoaluminophosphate with CHA topology), which is considered the archetypal system for industrial MTO processes[1]. The final spectra for SAPO-34 and SSZ-13 are almost identical, which confirms that the mechanistic insight is applicable to CHA topologies in general. The only noticeable difference between these catalysts is the temperature of hydrocarbon pool species formation (270 °C for SSZ-13 versus 300 °C for SAPO-34), which arises from the weaker acidity of the silicoaluminophosphate, as reported previously[23,39]. For completeness, Kerr-gated Raman spectroscopic data for the MTO process on SAPO-34 are provided (Supplementary Fig. 40), with additional characterization of the spent SSZ-13 (Supplementary Figs. 41,42).

Outlook

The unique combination of Kerr-gated Raman spectroscopy and molecular simulations allowed us to follow the formation of hydrocarbon species at various stages of methanol conversion (Fig. 6). From our results we conclude that the CHA topology deactivates rapidly owing to the tendency of extended polyenes to block the zeolite pores, which eventually undergo cyclization within the large chabazite cage, and lead to the formation of PAHs. We note that polyenes have been proposed previously as providers of the precursors to PAHs that lead to deactivation[32,40]. However, we provide unique mechanistic insight into how and why this occurs, and propose that this does not happen in the MFI structure owing to steric constraints that inhibit the cyclization of polyenes and PAHs within the pores and channel intersections, which leads to enhanced catalyst lifetime (Fig. 6). Previous studies demonstrated that SAPO-34 deactivation may start before substantial amounts of PAH form, which possibly arises from bulky products that are trapped in the large framework cavities[5]. Our findings demonstrate that it is the extended polyenes with no or small branches that are the crucial deactivating species that cause the onset of deactivation. As polyenes are typically produced through H-transfer reactions, higher reaction temperatures and/or diminished acid site densities should be beneficial, by favouring reactions such as cracking or reducing the rate of H-transfer. Nevertheless, to ultimately design a stable catalyst, steric effects also need to be considered fully.

Based on our findings, optimal MTO catalysts must present topological characteristics that are similar to those of chabazite (that is, 8-ring three-dimensional channels to retain shape selectivity, which maximizes light olefins production while enabling diffusion), ideally with smaller cavities that approach the size of MFI channel intersections, to inhibit intramolecular polyene cyclization. Materials that combine small cavities to prevent cyclization reactions and tailored acid sites to decrease the H-transfer rate will be less prone to deactivation through extended polyene formation and cyclization, and more competitive for the MTO process. An examination of the zeolite database suggests that there is perhaps only one 8-ring three-dimensional zeolite (known as MER) with the cage size and aspect ratio required to inhibit polyene cyclization. However, the combination of this topology being available with only a low Si/Al ratio and the comparatively narrow pore openings will likely affect the olefin product distribution[37]. Nowadays, hypothetical

databases exist that contain a huge numbers of structures for exploration; an examination of one database reveals a few interesting three-dimensional, 8-ring-containing candidate structures that potentially combine a restricted cage size and accessibility similar to that of CHA (3.8 Å) (Supplementary Fig. 43)[41,42]. However, the challenge is to make such structures, although our results indicate how insight that is derived from reaction mechanisms can provide a basis for targeted zeolite design (an approach that was advocated recently[12]); such insight, when combined with potential hypothetical structures, could allow the resolution of this 'polyene problem'. The understanding of a reaction mechanism lies at the heart of improving a catalyst's performance, which suggests that this approach could prove to be very powerful for revealing the 'mechanistic secrets' behind a range of catalytic reactions. The technique is not limited to catalysis, however, and could be applied easily to a range of functional materials.

Online content

Any methods, additional references, Nature Research reporting summaries, source data, extended data, supplementary information, acknowledgements, peer review information; details of author contributions and competing interests; and statements of data and code availability are available at https://doi.org/10.1038/s41563-020-0800-y.

Received: 27 September 2019; Accepted: 11 August 2020;
Published online: 14 September 2020

References

1. Olsbye, U. et al. Conversion of methanol to hydrocarbons: how zeolite cavity and pore size controls product selectivity. *Angew. Chem. Int. Ed.* **51**, 5810–5831 (2012).
2. Yarulina, I., Chowdhury, A. D., Meirer, F., Weckhuysen, B. M. & Gascon, J. Recent trends and fundamental insights in the methanol-to-hydrocarbons process. *Nat. Catal.* **1**, 398–411 (2018).
3. Yarulina, I. et al. Structure–performance descriptors and the role of Lewis acidity in the methanol-to-propylene process. *Nat. Chem.* **10**, 804–812 (2018).
4. Olsbye, U. et al. The formation and degradation of active species during methanol conversion over protonated zeotype catalysts. *Chem. Soc. Rev.* **44**, 7155–7176 (2015).
5. Hereijgers, B. P. C. et al. Product shape selectivity dominates the methanol-to-olefins (MTO) reaction over H-SAPO-34 catalysts. *J. Catal.* **264**, 77–87 (2009).
6. Bleken, F. et al. The effect of acid strength on the conversion of methanol to olefins over acidic microporous catalysts with the CHA topology. *Top. Catal.* **52**, 218–228 (2009).
7. Dahl, I. M. & Kolboe, S. On the reaction mechanism for hydrocarbon formation from methanol over SAPO-34: I. Isotopic labeling studies of the co-reaction of ethene and methanol. *J. Catal.* **149**, 458–464 (1994).
8. Dahl, I. M. & Kolboe, S. On the reaction mechanism for hydrocarbon formation from methanol over SAPO-34: 2. Isotopic labeling studies of the co-reaction of propene and methanol. *J. Catal.* **161**, 304–309 (1996).
9. Bjørgen, M. et al. Spectroscopic evidence for a persistent benzenium cation in zeolite H-beta. *J. Am. Chem. Soc.* **125**, 15863–15868 (2003).
10. McCann, D. M. et al. A complete catalytic cycle for supramolecular methanol-to-olefins conversion by linking theory with experiment. *Angew. Chem. Int. Ed.* **47**, 5179–5182 (2008).
11. Fu, H., Song, W. & Haw, J. F. Polycyclic aromatics formation in HSAPO-34 during methanol-to-olefin catalysis: ex situ characterization after cryogenic grinding. *Catal. Lett.* **76**, 89–94 (2001).
12. Li, C. et al. Synthesis of reaction-adapted zeolites as methanol-to-olefins catalysts with mimics of reaction intermediates as organic structure-directing agents. *Nat. Catal.* **1**, 547–554 (2018).
13. Arora, S. S., Nieskens, D. L. S., Malek, A. & Bhan, A. Lifetime improvement in methanol-to-olefins catalysis over chabazite materials by high-pressure H_2 co-feeds. *Nat. Catal.* **1**, 666–672 (2018).
14. Hunger, M., Seiler, M. & Buchholz, A. In situ MAS NMR spectroscopic investigation of the conversion of methanol to olefins on silicoaluminophosphates SAPO-34 and SAPO-18 under continuous flow conditions. *Catal. Lett.* **74**, 61–68 (2001).
15. Wang, W., Buchholz, A., Seiler, M. & Hunger, M. Evidence for an initiation of the methanol-to-olefin process by reactive surface methoxy groups on acidic zeolite catalysts. *J. Am. Chem. Soc.* **125**, 15260–15267 (2003).
16. Dai, W. et al. Understanding the early stages of the methanol-to-olefin conversion on H-SAPO-34. *ACS Catal.* **5**, 317–326 (2015).
17. Wang, C. et al. Experimental evidence on the formation of ethene through carbocations in methanol conversion over H-ZSM-5 zeolite. *Chem. Eur. J.* **21**, 12061–12068 (2015).
18. Chua, Y. T. & Stair, P. C. An ultraviolet Raman spectroscopic study of coke formation in methanol to hydrocarbons conversion over zeolite H-MFI. *J. Catal.* **213**, 39–46 (2003).
19. Beato, P., Schachtl, E., Barbera, K., Bonino, F. & Bordiga, S. Operando Raman spectroscopy applying novel fluidized bed micro-reactor technology. *Catal. Today* **205**, 128–133 (2013).
20. Signorile, M. et al. Topology-dependent hydrocarbon transformations in the methanol-to-hydrocarbons reaction studied by operando UV-Raman spectroscopy. *Phys. Chem. Chem. Phys.* **20**, 26580–26590 (2018).
21. Howe, R. F. et al. Reactions of dimethylether in single crystals of the silicoaluminophosphate STA-7 studied via operando synchrotron infrared microspectroscopy. *Top. Catal.* **61**, 199–212 (2018).
22. Qian, Q. et al. Combined operando UV/Vis/IR spectroscopy reveals the role of methoxy and aromatic species during the methanol-to-olefins reaction over H-SAPO-34. *ChemCatChem.* **6**, 3396–3408 (2014).
23. Borodina, E. et al. Influence of the reaction temperature on the nature of the active and deactivating species during methanol to olefins conversion over H-SSZ-13. *ACS Catal.* **5**, 992–1003 (2015).
24. Goetze, J. et al. Insights into the activity and deactivation of the methanol-to-olefins process over different small-pore zeolites as studied with operando UV–vis spectroscopy. *ACS Catal.* **7**, 4033–4046 (2017).
25. Lesthaeghe, D., Horré, A., Waroquier, M., Marin, G. B. & Van Speybroeck, V. Theoretical insights on methylbenzene side-chain growth in ZSM-5 zeolites for methanol-to-olefin conversion. *Chem. Eur. J.* **15**, 10803–10808 (2009).
26. Forester, T. R. & Howe, R. F. In situ FTIR studies of methanol and dimethyl ether in ZSM-5. *J. Am. Chem. Soc.* **109**, 5076–5082 (1987).
27. Stair, P. C. The application of UV Raman spectroscopy for the characterization of catalysts and catalytic reactions. *Adv. Catal.* **51**, 75–98 (2007).
28. Kim, H., Kosuda, K. M., Van Duyne, R. P. & Stair, P. C. Resonance Raman and surface- and tip-enhanced Raman spectroscopy methods to study solid catalysts and heterogeneous catalytic reactions. *Chem. Soc. Rev.* **39**, 4820–4844 (2010).
29. Matousek, P., Towrie, M., Stanley, A. & Parker, A. W. Efficient rejection of fluorescence from Raman spectra using picosecond Kerr gating. *Appl. Spectrosc.* **53**, 1485–1489 (1999).
30. Matousek, P., Towrie, M. & Parker, A. W. Fluorescence background suppression in Raman spectroscopy using combined Kerr gated and shifted excitation Raman difference techniques. *J. Raman Spectrosc.* **33**, 238–242 (2002).
31. Blaszkowski, S. R. & van Santen, R. A. The mechanism of dimethyl ether formation from methanol catalyzed by zeolitic protons. *J. Am. Chem. Soc.* **118**, 5152–5253 (1996).
32. Allotta, P. M. & Stair, P. C. Time-resolved studies of ethylene and propylene reactions in zeolite H-MFI by in-situ fast IR heating and UV Raman spectroscopy. *ACS Catal.* **2**, 2424–2432 (2012).
33. Socrates, G. *Infrared and Raman Characteristic Group Frequencies* 3rd edn (Wiley, 2004).
34. Ghysels, A. et al. Shape-selective diffusion of olefins in 8-ring solid acid microporous zeolites. *J. Phys. Chem. C* **119**, 23721–23734 (2015).
35. Tinnemans, S. J., Kox, M. H. F., Nijhuis, T. A., Visser, T. & Weckhuysen, B. M. Real time quantitative Raman spectroscopy of supported metal oxide catalysts without the need of an internal standard. *Phys. Chem. Chem. Phys.* **7**, 211–216 (2005).
36. Bjørgen, M. et al. Conversion of methanol to hydrocarbons over zeolite H-ZSM-5: on the origin of the olefinic species. *J. Catal.* **249**, 195–207 (2007).
37. *Database of Zeolite Structures* http://www.iza-structure.org/databases (2017).
38. Mores, D. et al. Space- and time-resolved in-situ spectroscopy on the coke formation in molecular sieves: methanol-to-olefin conversion over H-ZSM-5 and H-SAPO-34. *Chem. Eur. J.* **14**, 11320–11327 (2008).
39. Borodina, E. et al. Influence of the reaction temperature on the nature of the active and deactivating species during methanol-to-olefins conversion over H-SAPO-34. *ACS Catal.* **7**, 5268–5281 (2017).
40. Hwang, A., Kumar, M., Rimer, J. D. & Bhan, A. Implications of methanol disproportionation on catalyst lifetime for methanol-to-olefins conversion by HSSZ-13. *J. Catal.* **346**, 154–160 (2017).
41. Li, Y., Yu, J. & Xu, R. Criteria for zeolite frameworks realizable for target synthesis. *Angew. Chem. Int. Ed.* **52**, 1673–1677 (2013).
42. Li, Y. & Yu, J. New stories of zeolite structures: their descriptions, determinations, predictions, and evaluations. *Chem. Rev.* **114**, 7268–7316 (2014).

Methods

Catalyst synthesis. ZSM-5 zeolite (Si/Al = 15) was supplied by Zeolyst International in the ammonium form (CBV3024E), and the H-form of the zeolite material was obtained by calcination in air at 550 °C (2 °C min^{-1} to 120 °C and held for 30 min at this temperature, and then 5 °C min^{-1} to 550 °C and held for 12 h). SAPO-34 material is commercially available (ACS Material).

SSZ-13 zeolite (Si/Al = 15) was synthesized as described previously[43], but by using static conditions. The sample was calcined in air (1 °C min^{-1} to 120 °C and held for 2.5 h, 2.2 °C min^{-1} to 350 °C and held for 3 h, and finally 0.8 °C min^{-1} to 580 °C and held for 3 h). The identity and purity of the zeolite were verified by X-ray diffraction. Further characterization of the material (by X-ray diffraction analysis, chemical analysis, (27Al) NMR spectroscopy, ammonia temperature-programmed desorption analysis, scanning electron microscopy and Fourier transform infrared spectroscopy) is reported in a previous study[44] and is not repeated here.

Operando Kerr-gated Raman spectroscopy. The Kerr-gated Raman spectrometer at the ULTRA facility of the Central Laser Facility at the Rutherford Appleton Laboratory[31,32] was used. The laser source is a titanium sapphire laser that emits at 800 nm. The beam is frequency-doubled to 400 nm to produce the Raman probe beam. An average power of about 10 mW was delivered to samples in pulses of 3 ps at 10 kHz repetitions. The spot size of the beam at the sample was 100 µm and the sample was rastered to minimize sample damage caused by the beam. CS_2 was used as a Kerr medium and was activated by the fundamental 800 nm beam of the laser. The arrival time of the excitation pulse at the sample was adjustable with respect to the gating pulse. Several time delays were measured at each acquisition to ensure that the optimal Raman signal was measured. (See Supplementary Information for details on the ULTRA laser system and the Kerr gate set-up.)

The reaction was performed in a commercially available CCR1000 stage by Linkam Scientific. The cell consisted of a ceramic cup that held the solid catalyst on top of a ceramic fabric filter. This was placed inside a cell with quartz windows where an inner heating element controlled the temperature of the catalyst. The outer surface of the cell was cooled by a water cooling system. Gases entered a chamber in the cell where they flowed upwards and then down over the catalyst bed. The cell outlet gas was carried to a Pfeiffer OmniStar mass spectrometer for analysis of the reaction products.

A 50 mg quantity of catalyst was used in the experiments. Prior to the reaction, the catalyst was activated at 550 °C (5 °C min^{-1}) under a flow of 20% O_2 in He for 1 h. He gas was then flushed through the system to remove all O_2, and the catalyst was cooled to 100 °C. He was used as a carrier gas at a flow of 30 ml min^{-1}. Methanol was injected into the system by an HPLC pump that was set to 1.7 µl min^{-1} (corresponding to a weight of feed flowing per unit weight of the catalyst per hour of 1.6 $g_{methanol}\,g_{catalyst}^{-1}\,h^{-1}$), and flows were allowed to equilibrate by monitoring the signals from the mass spectrometer. Subsequently, the catalyst was heated up to 450 °C at a rate of 1 °C min^{-1}. After the experiment, the zeolite catalyst was cooled rapidly to 30 °C by the cooling system of the cell, to quench the reaction.

Prior to beginning the reaction, Raman spectra of the calcined catalyst samples were obtained by using five accumulations of 20 s exposure to give a total of 100 s of exposure time. During the reaction, one accumulation of 20 s exposure was used per measurement. This allowed a time resolution of 20 s for real-time investigation of the hydrocarbon pool intermediates. During temperature ramp experiments, measurements were taken every 10 °C.

Theoretical calculations. Molecular dynamics simulations were carried out with the CP2K simulation package (version 3.0)[45] at a density functional theory level combined with a GPW (Gaussian and plane wave) basis set[46]. The revPBE-D3 functional[47] with a DZVP (double-zeta valence polarized) basis set and GTH (Goedecker–Teter–Hutter) pseudopotentials were selected[48], as done previously[49], with a plane wave cut-off of 400 Ry. All simulations were performed in a periodic zeolite unit cell that represented a CHA topology containing 36 T sites and two Brønsted acid sites and that corresponded to a Si/Al ratio of 17, which is close to the experimental value of 15.

A large set of molecular dynamics simulations were performed that encompassed the empty zeolite, a methanol-loaded zeolite, and a broad variety of alkene, polyene and aromatic adsorbates (Supplementary Fig. 5). For each guest molecule, cell parameters were obtained by computing time-averaged values from a 50 ps NPT (amount N, pressure P and temperature T) molecular dynamics simulation at 350 °C and atmospheric pressure. The temperature and pressure were controlled by a chain of five Nosé–Hoover thermostats and an MTK (Martyna–Tobias–Klein) barostat, respectively[50]. An integration time step of 0.5 fs was applied. Production molecular dynamics runs that were used as input for the Raman spectra and mobility analysis were carried out in the NVT (amount N, volume V and temperature T) ensemble at 350 °C for 40 ps, preceded by an equilibration of 2.5 ps (see Supplementary Table 2 for the unit cell parameters).

Theoretical Raman spectra were obtained through Fourier transforms of the autocorrelation functions of the polarizability tensor[51]. Therefore, the polarizability tensor was derived every 2 fs through a finite difference approach[52] (see Supplementary Information for details).

Data availability

Source data are provided with this paper. Example CP2K input files and processing scripts are available from the public GitHub online repository at https://github.com/AlexanderHoffman/supporting-info. Owing to the large size of the molecular dynamics trajectories and CP2K output files, they are available upon author request instead.

References

43. Moliner, M., Franch, C., Palomares, E., Grill, M. & Corma, A. Cu–SSZ-39, an active and hydrothermally stable catalyst for the selective catalytic reduction of NO*x*. *Chem. Commun.* **48**, 8264–8266 (2012).
44. Lezcano-Gonzalez, I. et al. Determining the storage, availability and reactivity of NH_3 within Cu–chabazite-based ammonia selective catalytic reduction systems. *Phys. Chem. Chem. Phys.* **16**, 1639–1650 (2014).
45. Hutter, J., Iannuzzi, M., Schiffmann, F. & VandeVondele, J. CP2K: atomistic simulations of condensed matter systems. *Wiley Interdiscip. Rev. Comput. Mol. Sci.* **4**, 15–25 (2014).
46. Lippert, G., Hutter, J. & Parrinello, M. The Gaussian and augmented-plane-wave density functional method for ab initio molecular dynamics simulations. *Theor. Chem. Acc.* **103**, 124–140 (1999).
47. Yang, K., Zheng, J., Zhao, Y. & Truhlar, D. G. Tests of the RPBE, revPBE, τ-HCTHhyb, ωB97X-D, and MOHLYP density functional approximations and 29 others against representative databases for diverse bond energies and barrier heights in catalysis. *J. Chem. Phys.* **132**, 164117 (2010).
48. Goedecker, S., Teter, M. & Hutter, J. Separable dual-space Gaussian pseudopotentials. *Phys. Rev. B* **54**, 1703–1710 (1996).
49. Cnudde, P. et al. How chain length and branching influence the alkene cracking reactivity on H-ZSM-5. *ACS Catal.* **8**, 9579–9595 (2018).
50. Frenkel, D. & Smit, B. *Understanding Molecular Simulation* 2nd edn (Academic Press, 2002).
51. Luber, S., Iannuzzi, M. & Hutter, J. Raman spectra from ab initio molecular dynamics and its application to liquid *S*-methyloxirane. *J. Chem. Phys.* **141**, 094503 (2014).
52. Thomas, M., Brehm, M., Fligg, R., Vöhringer, P. & Kirchner, B. Computing vibrational spectra from ab initio molecular dynamics. *Phys. Chem. Chem. Phys.* **15**, 6608–6622 (2013).

Acknowledgements

This research has been performed with the use of facilities including a Raman spectrometer and thermogravimetric analysis equipment at the Research Complex at Harwell. We thank the Research Complex for access and support to these facilities and equipment. We acknowledge the Engineering and Physical Sciences Research Council for funding grants EP/K007467/1, EP/K014706/2, EP/K014668/1, EP/K014854/1, EP/K014714/1, EP/M013219/1, EP/S016481/1 and EP/S016481/1. The Science and Technology Facilities Council (STFC) is acknowledged for the beam time at the ULTRA facility for performing Kerr-gate experiments. L. Mantarosie (Johnson Matthey PLC) is also thanked for her assistance and expertise. P. Matousek and T. Parker (STFC) are acknowledged for useful discussions. V.V.S., A.E.J.H. and M.B. acknowledge the Research Foundation – Flanders (FWO), the Special Research Fund of Ghent University, and funding from the Horizon 2020 research and innovation program of the European Union (consolidator European Research Council grant agreement no. 647755 – DYNPOR (2015–2020)). The computational resources and services were provided by Ghent University (Stevin Supercomputer Infrastructure) and the Flemish Supercomputer Center, and funded by the FWO.

Author contributions

I.L.-G. and A.M.B. conceived and coordinated the project with V.V.S., M.T. and I.V.S. as close collaborators. I.L.-G. performed the operando Kerr-gated Raman experiments, and E.C., M.A.-A., E.K.G., A.G. and I.V.S. supported the work. A.E.J.H., M.B., K.d.W. and V.V.S. performed the molecular simulations. I.L.-G., E.C., A.E.J.H., V.V.S., K.d.W., A.M.B., M.T. and I.V.S. contributed to the data analysis and discussion. I.L.-G., E.C., A.E.J.H., V.V.S. and A.M.B. wrote the manuscript with input from all authors.

Competing interests

The authors declare no competing interests.

Additional information

Supplementary information is available for this paper at https://doi.org/10.1038/s41563-020-0800-y.

Correspondence and requests for materials should be addressed to I.L.-G., V.V. or A.M.B.

Reprints and permissions information is available at www.nature.com/reprints.